

Ultrasound-Based Estimation of Fibre-Directional Strain

Citation for published version (APA):

Fixsen, L. S., & Lopata, R. G. P. (2022). Ultrasound-Based Estimation of Fibre-Directional Strain: A Simulation Study. *Ultrasound in Medicine and Biology*, 48(9), 1785-1796.
<https://doi.org/10.1016/j.ultrasmedbio.2022.05.004>

Document license:
CC BY

DOI:
[10.1016/j.ultrasmedbio.2022.05.004](https://doi.org/10.1016/j.ultrasmedbio.2022.05.004)

Document status and date:
Published: 01/09/2022

Document Version:
Publisher's PDF, also known as Version of Record (includes final page, issue and volume numbers)

Please check the document version of this publication:

- A submitted manuscript is the version of the article upon submission and before peer-review. There can be important differences between the submitted version and the official published version of record. People interested in the research are advised to contact the author for the final version of the publication, or visit the DOI to the publisher's website.
- The final author version and the galley proof are versions of the publication after peer review.
- The final published version features the final layout of the paper including the volume, issue and page numbers.

[Link to publication](#)

General rights

Copyright and moral rights for the publications made accessible in the public portal are retained by the authors and/or other copyright owners and it is a condition of accessing publications that users recognise and abide by the legal requirements associated with these rights.

- Users may download and print one copy of any publication from the public portal for the purpose of private study or research.
- You may not further distribute the material or use it for any profit-making activity or commercial gain
- You may freely distribute the URL identifying the publication in the public portal.

If the publication is distributed under the terms of Article 25fa of the Dutch Copyright Act, indicated by the "Taverne" license above, please follow below link for the End User Agreement:

www.tue.nl/taverne

Take down policy

If you believe that this document breaches copyright please contact us at:

openaccess@tue.nl

providing details and we will investigate your claim.

● Original Contribution

ULTRASOUND-BASED ESTIMATION OF FIBRE-DIRECTIONAL STRAIN: A SIMULATION STUDY

LOUIS S. FIXSEN, and RICHARD G.P. LOPATA

Department of Biomedical Engineering, Eindhoven University of Technology, Eindhoven, The Netherlands

(Received 1 July 2021; revised 13 April 2022; in final form 5 May 2022)

Abstract—Left ventricular (LV) strains are typically represented with respect to the imaging axes. Contraction within the myocardium occurs along myofibres, which vary in orientation. Therefore, a mismatch exists between the direction in which strain is calculated and that in which contraction occurs. In this study, ultrasound-based fibre orientation and 3-D strain estimation were combined to calculate the fibre-directional strain. Three-dimensional ultrasound volumes were created by simulating simple geometrical phantoms and a phantom based on a finite-element (FE) model of LV mechanics. Fibre-like structures were embedded within tissue-mimicking scatterers. Strains were applied to the numerical phantom, whereas the FE phantom was deformed based on the LV model. Fibre orientation was accurately estimated for both phantoms. There was poor agreement in axial and elevational strains (root mean square error = 29.9% and 12.3%), but good agreement in lateral and fibre-directional strains (root mean square error = 6.4% and 5.9% respectively), which aligned in the midwall. Simplifications to reduce computational complexity caused poor axial and elevational strain estimation. However, calculation of fibre-directional strain from single-modality ultrasound volumes was successful. Further studies, in *ex vivo* setups because of the fundamental limitations of currently available transducers, are needed to verify real-world performance of the method. (E-mail: l.s.fixsen@tue.nl) © 2022 The Author(s). Published by Elsevier Inc. on behalf of World Federation for Ultrasound in Medicine & Biology. This is an open access article under the CC BY license (<http://creativecommons.org/licenses/by/4.0/>).

Key Words: Ultrasound simulation, Strain imaging, Speckle tracking, Fibre orientation, Backscatter tensor imaging.

INTRODUCTION

Ultrasound strain imaging allows for the non-invasive estimation of strain, the change in length between pre-determined points within a region of tissue, in two and three dimensions in the heart (Chen et al. 2005; Amundsen et al. 2006; Crosby et al. 2009). Parameters obtained through strain imaging, particularly global strains, have been found to be earlier indicators of impaired ventricular function when compared with the more commonly used left ventricular ejection fraction (Stanton et al. 2009). LV strains are typically calculated in the longitudinal, circumferential and transmural directions, as (if simplified into an ellipsoid) these are equivalent to deformation that occurs in the primary axes of the left ventricle (LV).

Global strain is calculated as the average strain that occurs throughout multiple segments in each axis of the LV (Voigt et al. 2015). However, deformation of the myocardium occurs as a result of the contraction and relaxation of sarcomeres, which are made up of fibre-like cardiac muscle cells, so-called cardiomyocytes (Ho 2009). Individual myocytes are around 120 μm long and 20–30 μm thick (Ho 2009). The fibres are themselves tightly bonded into sheets, or laminae, that are around four cells thick (Legrice et al. 1997) and are separated by cleavage planes. Deformation occurs along the length of the myocytes, meaning that for the efficient ejection of blood from the ventricle, the orientation of these cells varies throughout the wall (Hansen et al. 1991; Bovendeerd et al. 1994; Taber et al. 1996). This results in a complex helical arrangement of myofibres (muscle fibres), with the orientation varying smoothly in all axes, primarily in the longitudinal and circumferential directions (LeGrice et al. 1995; Legrice et al. 1997). Therefore, there is a mismatch between the axis in which strain actively occurs (*i.e.*, the

Address correspondence to: Louis S. Fixsen, Department of Biomedical Engineering, Eindhoven University of Technology, PO Box 513, 5600 MB Eindhoven, The Netherlands. E-mail: l.s.fixsen@tue.nl

fibre-directional strain) and the axes in which strains can be calculated using ultrasound strain imaging. Furthermore, strain along the fibre direction may be more physiologically relevant when characterising local tissue function.

Spatial averaging of strain, as used in the measurement of global strains, is common and necessary because of the large number of local errors that occur in strain estimation caused by poor signal-to-noise ratio (SNR), imaging artefacts and out-of-plane motion. These errors reduce the accuracy of inter-frame displacement tracking that is performed prior to strain calculation and, in turn, influence the final estimate. However, this averaging also leads to the loss of information on the local function of tissue.

There has been much interest in the non-invasive mapping of cardiac myofibre orientation (Watson et al. 2018). Recently, a method was developed that can be used to estimate the orientation of fibrous structures in ultrasound data, in both two (Papadacci et al. 2014) and three (Papadacci et al. 2017) dimensions, by calculating the spatial coherence of received signals. By calculating the similarity of received signals across the transducer elements, the degree of (an)isotropy in the medium can be determined accurately, as can the in- and out-of-plane (Turquin et al. 2019) directionality of the signals. This technique, termed *3-D backscatter tensor imaging* (3-D BTI), has possible utility in determining the amount of disarray in the arrangement of the muscle, for example, by detecting scarring of the muscle caused by an infarct.

We hypothesised that the physiological relevance of ultrasound strain estimation could be improved by combining strain estimation in 3-D with the local estimation of the myofibre orientation, thereby obtaining the strain that occurs in the fibre direction. This “fibre-directional strain” could potentially be used to mitigate errors that occur because of incorrect placement of the ultrasound probe by standardising strain directions and, furthermore, give information on the activation of the heart muscle and (remaining) ventricular function.

In this study, the fundamental basis for the technique is investigated in ultrasound simulations. After the method is validated in a series of simple strain phantoms, the accuracy of both strain and fibre orientation estimation was investigated on data created using a realistic, 3-D, finite-element model of the left ventricle.

METHODS

Ultrasound simulations

Simulations were performed to generate the 3-D volumes of radiofrequency (RF) ultrasound required for the fibre orientation and strain analysis. The simulations were performed in MATLAB (version 2019b, The

MathWorks, Natick, MA, USA), using the Field II simulation framework (Jensen and Svendsen 1992; Jensen 1996). A 1024-element 2-D matrix array (*i.e.*, 32×32 elements) with 300- μm pitch was modelled, based on the Vermon 1024 EL ultrasound probe (Vermon S.A., Tours, France) used for similar *in vitro* and *ex vivo/in vivo* studies (Papadacci et al. 2017; Ramalli et al. 2019; Turquin et al. 2019). This resulted in an aperture size of 9.6 mm \times 9.6 mm. A 3-MHz centre frequency and 30-MHz sampling frequency were used. The spatial impulse response was a 2.5-cycle Hamming-weighted sinusoidal pulse, and the aperture excitation function was a single-cycle Hamming-weighted sinusoidal pulse.

Each image volume (*i.e.*, simulated time point) was created by the transmission and reception of 25 steered plane waves. The direction of each wave was determined by two angles, with each angle ranging between -6° and $+6^\circ$, and an increment of 3° . The simulated RF signals were reconstructed into a complete volume on an Nvidia GPU using custom software implemented in MATLAB and CUDA. The signals were coherently compounded on a grid with an axial spacing of 50 μm and lateral/elevational spacing of 300 μm . The reconstructed volumes had a lateral and elevational size of 19.2×19.2 mm (*i.e.*, 65 samples in each direction). The axial size of the volumes varied between 20 and 30 mm, and was large enough to encompass the range of positions between which the simulated phantoms would move.

In silico phantoms

Two numerical phantoms were created to validate both fibre orientation and strain estimation: firstly, an ideal phantom embedded with fibres that were deformed in each imaging axis separately; and secondly, a phantom with both fibre orientation distribution and deformation given by a finite-element (FE) model of left ventricular mechanics (Fig. 1A). Full details of the model parameters used in the finite-element simulation can be found in Table 1 of Bovendeerd et al. (2009). In both cases, the phantoms were positioned with the major fibre axis perpendicular to the ultrasound beam axis, in an idealised case of a real-world parasternal short- or long-axis echo.

The basic design was the same for each phantom and was based on previous work by Ramalli et al. (2018), with the most significant additional contributions being a more realistic transmural fibre orientation distribution, the addition of motion/deformation and out-of-plane fibre orientations.

Two sets of scatterers, both with a density of 8×10^6 scatterers/ cm^3 , were placed in the same volume: randomly placed scatterers with a Gaussian amplitude distribution to replicate the diffuse reflections of

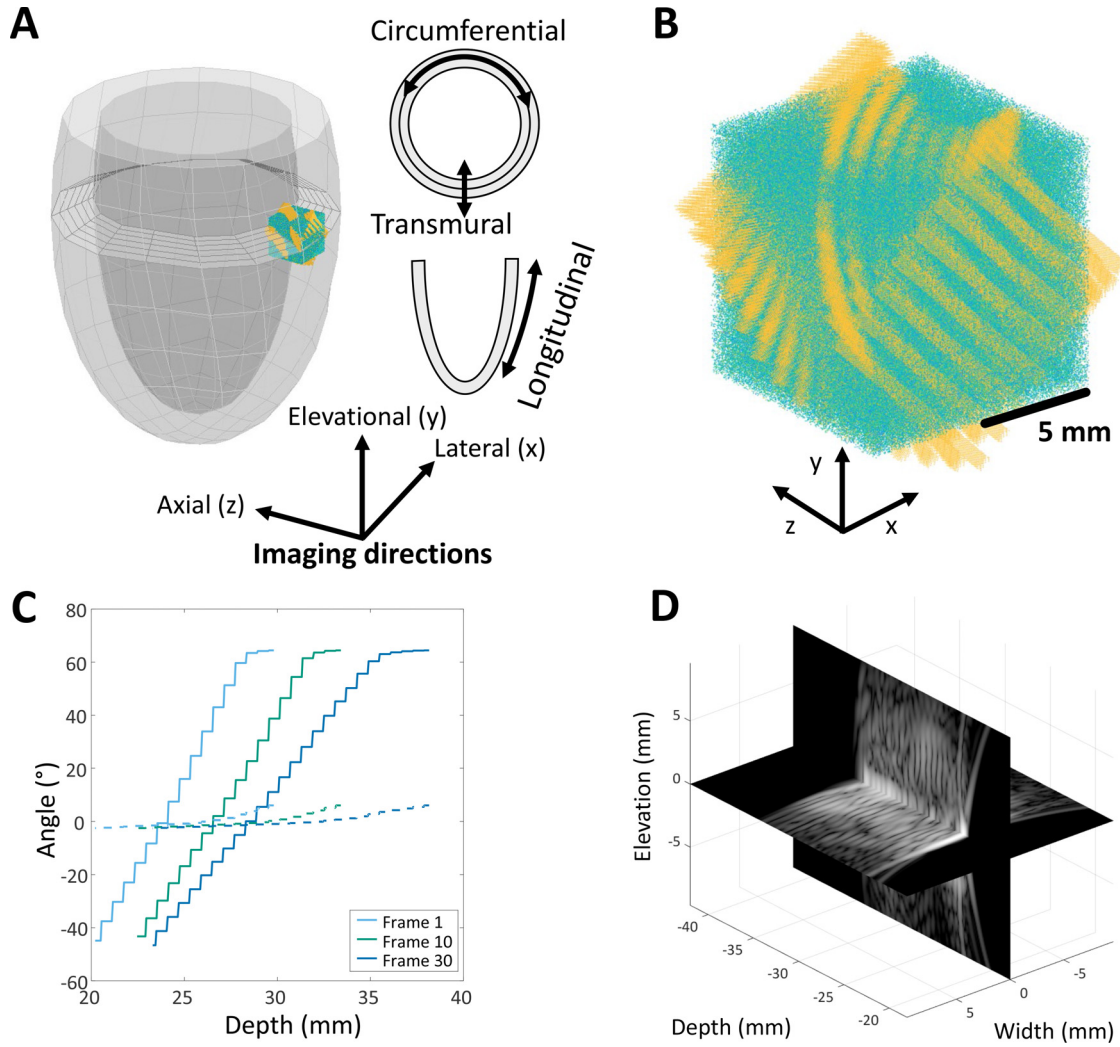


Fig. 1. (A) Left ventricle (LV) mesh and block of scatterers used in simulations, positioned at the midlevel of the LV wall, illustrating the directions in which LV strains are calculated (circumferential, transmural and longitudinal) and imaging directions of the present study (axial, lateral and elevational). (B) Ultrasound phantom, made up of scatterers that return coherent (yellow-colored) and incoherent (turquoise-colored) signals. (C) Plot revealing change in fibre angle over depth for three of the simulated time points. Solid lines represent the in-plane angle, and dashed lines, the out-of-plane angle. (D) Reconstructed B-mode ultrasound volume at frame 10.

ultrasound signals in tissue; and evenly spaced scatterers of an equal amplitude to replicate the specular reflection of ultrasound by the cardiac myofibres/sheets. The influence of different speckle amplitudes on the accuracy of

Table 1. Applied and estimated strains in each imaging axis*

Applied strain (%)			Measured strain (%)		
Axial	Lateral	Elevational	Axial	Lateral	Elevational
3	0	0	2.90	1.16	1.81
-3	0	0	-2.99	-1.27	-1.60
0	3	0	0.03	2.66	-0.14
0	-3	0	-0.02	-2.27	0

* Strains were applied to the ideal phantom and estimated through 3-D strain imaging on the simulated ultrasound data.

the orientation estimation was assessed (details of this analysis can be found in the Results). The mean amplitude of the tissue scatterers was set 10 dB below that of the fibre scatterers, such that both fibre estimation and displacement estimation could be performed on the simulated volumes.

The scattering amplitude η of the coherent fibres was specified according to a periodic function:

$$\eta(x) = III_P(x) \otimes \Pi\left(\frac{x}{S}\right) \quad (1)$$

Here, III_P denotes the Dirac comb function of period P , where P is the fibre pitch, and Π denotes the rectangular function, with S the fibre size. In all simulations, the values of these parameters were set to $P = 1200 \mu\text{m}$ and

$S = 600 \mu\text{m}$. This was the smallest fibre size and period that could be resolved when the out-of-plane rotation of fibres was included, given the density of scattering particles used in the present model. A greater scatterer density would allow for smaller fibres to be modeled, at the expense of increased computational load (using the present simulation framework). It should be noted that individual myocytes are significantly smaller than this, around $120 \mu\text{m}$ long and $20\text{--}30 \mu\text{m}$ thick (Ho 2009), and are more tightly arranged. Whether the spatial resolution obtained with the present transmission and compounding methods would allow for the orientation of smaller structures to be resolved, such as myocytes or laminae, was not investigated in this study, given the aforementioned computational limitation (this subject is explored further under Limitations in the Discussion). However, Papadacci et al. (2017) previously reported that similar transmission and compounding methods allowed for measurement of fibre direction in real myocardium.

The periodic function is sampled on a single line of points x with amplitude 0 or 1. This was replicated in the y - and z -axes, resulting in a mask denoting the scatterer amplitudes. This amplitude mask was applied to an evenly spaced grid of scatterers with a spacing of $50 \mu\text{m}$. To replicate the transmural variation in myofibre orientation, for the ideal phantom, the in-plane (*i.e.*, x - y) angle θ was determined by

$$\theta(z) = \theta_0 \times \frac{\partial\theta}{\partial z} \times \left\lceil \frac{z - \frac{S}{2}}{S} \right\rceil \quad (2)$$

where θ_0 is the initial fibre angle and $\partial\theta/\partial z$ is the fibre orientation rate of change transmurally (*i.e.*, in the axial direction). Therefore, the in-plane fibre angle changes incrementally over the depth of the phantom, with the angle increment dependent on the thickness of the fibre “sheet.” With the orientation of each sheet known for a given depth, the scatterer positions were multiplied with a rotation matrix. Finally, the amplitude mask was used to remove all scatterers with an amplitude of 0 to reduce the simulation time. The ideal phantom was $10 \text{ mm} \times 10 \text{ mm} \times 6 \text{ mm}$ in size, with $\theta_0 = -75^\circ$ and $\partial\theta/\partial z = 25^\circ/\text{mm}$. Approximately 7.1×10^6 scatterers were used, of which 2.3×10^6 scatterers made up the fibre sheets, with the remaining 4.8×10^6 scatterers mimicking the diffuse scattering by the tissue.

For validation of the fibre-directional strain imaging method used in this study, additional simulations were performed after positive and negative strains of 3% were applied to the scatterers in the lateral and axial directions in a single deformation step. This strain magnitude was selected based on the greatest inter-frame strain magnitude that would occur in the FE-based phantom, with the simulated frame rate (81 Hz). For ultrafast imaging, the inter-frame strain rate would be even lower.

In the FE-based phantom, the in-plane and out-of-plane fibre angles (θ and φ , respectively) of the phantom were calculated by mapping the vector specifying the fibre orientation (in the x - y and z - y planes) for each mesh node in the region the phantom was positioned in (Fig. 1B, 1C). The transmural angle distribution was then interpolated over the z -coordinates of the phantom. As in the ideal phantom, the increment in the orientation was dependent on the fibre thickness. In addition to the in-plane rotation, each fibre sheet with angle θ was subsequently rotated by the out-of-plane angle φ . θ varied between -45° at the epicardial boundary and 65° at the endocardial boundary, while φ varied between -2.5° and 6° . The orientation variation is a subset of the fibre angles illustrated in Bovendeerd et al. (2009) (Fig. 1), with the in- and out-of-plane equivalent to α_h and α_t respectively.

The FE phantom was $10 \times 10 \text{ mm}$ wide with a thickness ranging between 9.5 mm at end-diastole and 14.9 mm at end-systole. To maintain the coherent response of the embedded fibres, the fibre sheets were regenerated for each volume. The underlying tissue was deformed according to the FE model. A total of 12×10^6 scatterers were used in the FE phantom for the first simulated volume; the last volume was made up of 14×10^6 scatterers because of the elongation of the phantom in the axial direction.

The FE phantom was simulated at a volume rate of 81 Hz over the systolic period, resulting in 30 volumes between end-diastole (*i.e.*, end filling, frame 1) and end-systole (*i.e.*, end ejection, frame 30). Next, the generated tissue scatterers were placed inside the LV mesh at the midlevel of the ventricle, and a convex hull was used to remove any scatterers that were outside the mesh boundary. Finally, the inter-frame displacements of the mesh nodes were interpolated across the scatterers.

Spatial coherence

The ultrasonic spatial coherence was computed from the reconstructed volumes for every time point simulated (Fig. 1D), according to the method outlined by Papadacci et al. (2017). A map of the spatial coherence within a certain temporal window (*i.e.*, over a given depth range) was obtained by autocorrelating the signals received by successive pairs of elements. The coherence function $R(\Delta x, \Delta y)$ was therefore expressed as a function of the distance between elements

$$R(\Delta x, \Delta y) = \frac{1}{N_x - |\Delta x|} \frac{1}{N_y - |\Delta y|} \sum_{x_i} \sum_{y_i} \frac{\sum_{t=T_1}^{T_2} S_{\text{RF}}(x_i, y_i, t) \cdot S_{\text{RF}}(x_i - \Delta x, y_i - \Delta y, t)}{\sqrt{\sum_{t=T_1}^{T_2} S_{\text{RF}}(x_i, y_i, t)^2 \cdot \sum_{t=T_1}^{T_2} S_{\text{RF}}(x_i - \Delta x, y_i - \Delta y, t)^2}} \quad (3)$$

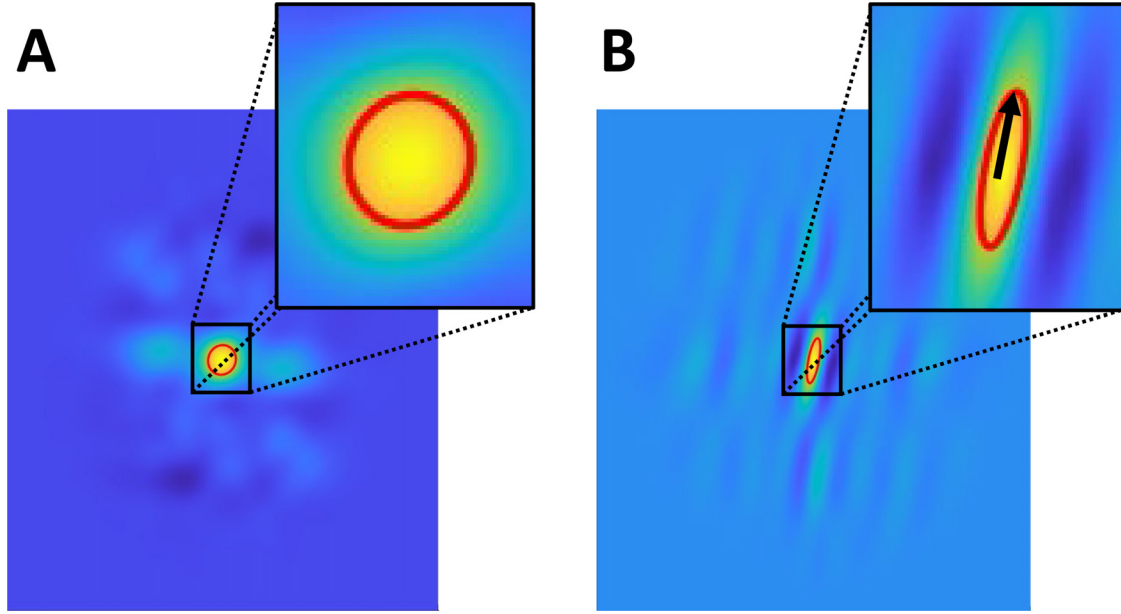


Fig. 2. (A) Interpolated coherence map acquired in a region of speckle. The random positioning and Gaussian amplitude distribution produce a spatially incoherent result, yielding an almost completely circular ellipse. (B) Interpolated spatial coherence map acquired in a region of fibre-like scatterers, which produce a coherent response because of the similar phase and amplitude of the received signals. The *red ellipse* is fitted to the center of the image, with the *arrow* denoting the major axis (L) of the ellipse.

where S_{RF} is the signal received by an element i that is positioned at x_i and y_i . Δx and Δy are the distances in the main coordinate axes of the 2-D array between element i and another element. The coherence is averaged over the temporal window between T_1 and T_2 . N_x and N_y represent the number of elements in the x- and y-axes, respectively. A temporal window of $2.57 \mu s$ was used, that is, 50 samples at the sampling frequency given.

Notably, N_x and N_y can be made up of a subset of the total elements in the transducer which can be combined with a sliding window in both x- and y-axes. This allows for estimation of multiple spatial coherence maps at any given depth and the estimation of different fibre orientations within the x–y plane. However, given the small transducer footprint and alignment of fibres at a given depth, this was not performed in this study.

The 3-D map of spatial coherence over depth was then used to estimate the orientation and anisotropy of structures in the reconstructed ultrasound volume. According to the Van Cittert–Zernicke theorem (Mallart and Fink 1991), in a completely random medium, for instance in fully developed speckle, the coherence is given by the spatial Fourier transform of the ultrasound intensity distribution in the focal plane.

For a 2-D matrix array, as was simulated in this study, this would be equal to a 2-D sinc function and result in a superelliptical-shaped spatial coherence map. Essentially, the isotropy of the medium leads to a similar

coherence value in all directions (Fig. 2A), with slightly greater coherence values extending in the major axes of the transducer. In contrast, in an anisotropic medium, signals will correlate more in the direction that aligns with the orientation of any structures in the region (Fig. 2B).

Therefore, by analysing the shape of the spatial coherence map it is possible to determine both the (an) isotropy and orientation of structures in the region of interest. An ellipse was fitted to the centre of a mask, created by thresholding the spatial coherence map to 75% of its maximum value. The fitted ellipse provides information on the orientation of the spatial coherence through the angle (α), relative to the x-axis, of its major axis, with possible values of α falling between -90° and 90° .

Furthermore, the fractional anisotropy (FA) of the ellipse for a given depth could be obtained (Özarslan et al. 2005) as

$$FA = \sqrt{2 \cdot \frac{(L - \bar{l})^2 + (l - \bar{l})^2}{L^2 + l^2}} \quad (4)$$

where L , \bar{l} and l are the major axis length, mean axis length and minor axis length of the ellipse, respectively. If the medium is isotropic, then $FA \rightarrow 0$ because the major and minor axis lengths become more equal and thus approach the mean axis length. Whereas if $FA \rightarrow 1$, the major axis is significantly longer than the minor axis and the medium is more anisotropic. This provides a

measure of the reliability of angle estimates at a given depth, with a minimum FA of 0.3 used henceforth.

3-D strain imaging

The reconstructed volumes were separately processed using a strain imaging toolbox, implemented in MATLAB and developed by Lopata et al. (2009, 2011). The 3-D displacement tracking algorithm of (Lopata et al. 2011) was used with some modifications. Specifically, the phantom was tracked using a single iteration 3-D displacement tracking algorithm. The cross-correlation of a rigid kernel of 3-D RF data ($2.7 \times 2.7 \times 2.3$ mm) within a larger search region ($3.3 \times 3.3 \times 4.7$ mm) yielded the inter-frame displacements of different regions of the volume, with 3-D parabolic interpolation used to calculate subsample displacement estimates. The results of the cross-correlation were separated into displacements in the lateral, elevational and axial directions in the imaging plane (equivalent to the circumferential, longitudinal and radial LV directions in the volume simulated) and smoothed with a median filter.

A tracking mesh of 20 axial, 10 lateral and 10 elevational points was created within the tracked region for the first frame. The inter-frame displacements were interpolated across the generated tracking points for each subsequent frame and added cumulatively to the points. Normal and shear strains in each axis were calculated by taking the spatial derivative of the tracking mesh relative to its initial geometry, using a 3-D least-squares strain estimator (Lopata et al. 2011).

Furthermore, the principal and fibre-directional strains were calculated. The principal strains were found by calculating the eigenvalues of the Green–Lagrange strain tensor E (formed from the normal and shear strains), with the principal directions being the resulting eigenvectors. These were obtained using the *eig* function in MATLAB, which solves the equation

$$(E - \lambda I) \cdot v = 0 \quad (5)$$

with λ the eigenvalues (ee_1 , ee_2 and ee_3), I the identity matrix and v the eigenvectors from the Green–Lagrange strain tensor E . To calculate the fibre-directional strain e_{fib} , the in-plane angle α estimated over the depth of the volume was converted into a direction vector v and interpolated over the tracked mesh. The out-of-plane angle was assumed to be 0° , as only the in-plane (x–y) fibre orientation was estimated from the 3-D spatial coherence data:

$$e_{\text{fib}} = v^T \cdot E \cdot v \quad (6)$$

Statistics

Error between ground truth and estimated fibre orientation and strains was assessed by calculating the root-mean-square error (RMSE) over the simulated time

period (*i.e.*, systole). The RMSE is given as absolute values, degrees ($^\circ$) and percentage strain (%); that is, an RMSE of 5% is equal to an error of 5% strain, not 5% of the strain magnitude. Additionally, the similarity between ground truth and estimated strains was assessed with Pearson's correlation (r).

RESULTS

Ideal phantom

The accuracy of displacement tracking and strain estimation was first assessed by applying a strain of $\pm 3\%$ to the ideal phantom in the axial and lateral directions. Table 1 outlines the results of the strain estimation. Strain magnitudes close to the applied positive and negative strains were estimated in the axial direction. However, there was a large erroneous strain estimated in both lateral and elevational directions (as expected because of the lower imaging resolution in these directions). In contrast, while applied positive and negative lateral strains were underestimated to a greater extent (2.66% and -2.27% respectively), erroneous strains were markedly lower (maximum of 0.14% in the elevational direction).

In the ideal phantom, the RMSE between the ground-truth and estimated (in-plane) fibre orientations was 6.66° . Figure 3 (*dashed lines*) illustrates both the ground truth angle and fibre-directional strain over the depth of the phantom; the estimated angle (straight line) closely follows the ground truth value, although the step-wise change in angle of the ground truth is not reflected in the estimated values.

The fibre-directional strain calculation was validated by finding the proportion of strain that occurred in the estimated fibre orientation (Fig. 3, *straight lines*). Fibre-directional strain magnitude for the lateral directions was greatest, and equal to the applied strain, when the fibre angle aligned with the x-axis (*i.e.*, the angle was at or close to 0°). Non-zero fibre-directional strains were estimated after strains were applied in the axial direction. Compared with the ground truth, whilst minimum and maximum lateral fibre-directional strain is estimated with low error, the strain over the depth has a higher gradient (*i.e.*, greater error), leading to over- and underestimation of the strain. The error bars indicate that, in general, the error in fibre directional strain was greatest at the start and end of the phantom.

Finite-element model-based phantom

The influence of the background speckle on the accuracy of fibre orientation estimation in the FE phantom was investigated by simulating phantoms with the mean speckle amplitude at 0, -10 and -20 dB relative to the amplitude of the fibres (Fig. 4). With speckle at 0 dB, the RMSE between the ground truth and estimated

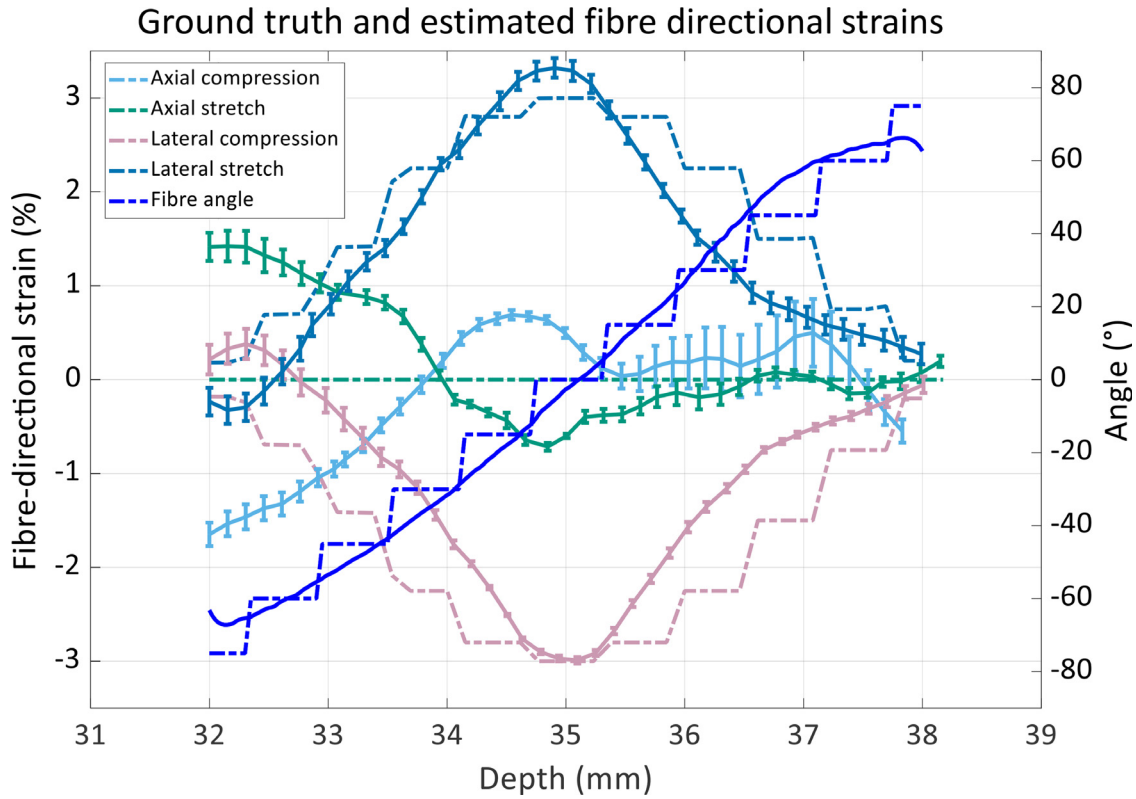


Fig. 3. Ground truth (*dashed lines*) and estimated (*straight lines*) fibre orientation and fibre-directional strain in the ideal phantom (note the ground truth axial compression line covered by axial stretch). *Error bars* represent the standard deviation in fibre-directional strain at a given depth.

angle was 11.1° , while FA was below 0.3 for much of the phantom. For simulations with speckle at -10 and -20 dB, both RMSE and regions with low FA were similar (RMSE = 5.03° and 4.98° , respectively).

Normal, fibre and principal strains were calculated from displacements obtained from the ground truth (the phantom) and simulated ultrasound data (Fig. 5). Elevational and axial (e_y and e_z) strains were greatly underestimated, shown through poor correlation and high RMSE relative to the ground truth (e_y , $r = 0.34$, RMSE = 12.3% ; e_z , $r = 0.51$, RMSE = 29.9%). Conversely, lateral and fibre strains correlated well with

relatively low error (e_x , $r = 0.80$, RMSE = 6.35% ; e_{fib} , $r = 0.88$, RMSE = 5.85%). When taken as the mean strain within the entire region of interest, e_x and e_{fib} were similar in shape and magnitude for both the ground truth and simulated data.

There was good agreement between ground truth and estimated principal strains. The mean and standard deviation in angular distance between ground truth and estimated principal directions was calculated over the simulated period. The angular distance for the first principal direction was $53^\circ \pm 17^\circ$, the second $75^\circ \pm 16^\circ$ and the third $71^\circ \pm 21^\circ$. If only overlapping portions of the

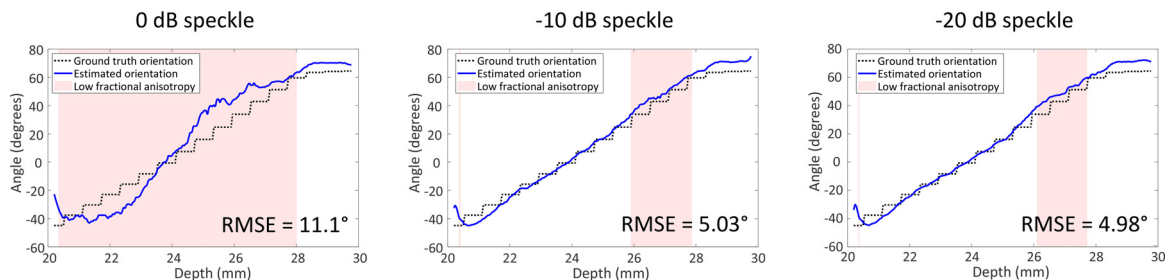


Fig. 4. Influence of speckle amplitude on the accuracy of the fibre orientation estimation. *Pink-shaded areas* are estimates for which the fractional anisotropy was below the threshold of 0.3.

Ground truth and estimated strains

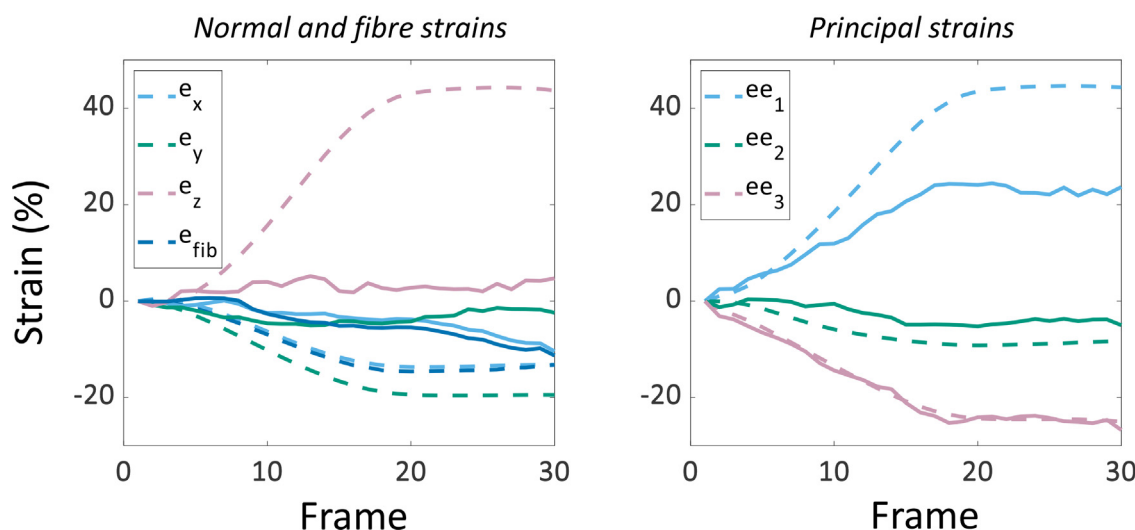


Fig. 5. Strain during systole calculated from ground truth (*dashed lines*) and simulated data (*straight lines*), indicating strain in each axis (e_x , e_y and e_z), fibre-directional strain (e_{fib}), and the first, second and third principal strains (ee_1 , ee_2 and ee_3 , respectively).

tracking mesh are taken into account, then the distance reduces to $36^\circ \pm 11^\circ$ for the first principal direction. There was no improvement for the second and third principal directions. Strain curve correlation was good for all directions, particularly the first and third principal strains (ee_1 , $r = 0.99$; ee_2 , $r = 0.90$; ee_3 , $r = 0.99$). RMSE was highest for the first principal strain (ee_1 , RMSE = 15.0%). RMSE for the second principal strain was high relative to the overall low strain amplitude (ee_2 , RMSE = 3.93%). RMSE for the third principal strain was low (ee_3 , RMSE = 0.86%).

Ground truth and estimated fibre angles exhibited good agreement during systole (Fig. 6, left-hand plots), although estimated strains are noisier. Transmural ground truth fibre-directional strains had the greatest magnitude at the epicardial and endocardial borders, with a region of lower strain magnitude in the central myocardium. Estimated fibre-directional strains exhibit poor overall tracking of wall motion during systole, with no endocardial fibre-directional strain estimated (because of underestimated axial displacements). Epicardial fibre-directional strains were closer to the ground truth, but underestimated.

DISCUSSION

In this study we found that measurement of fibre-directional strain is feasible through the combination of measurements from two 3-D ultrasound image analysis techniques, strain imaging and backscatter tensor imaging. The feasibility of the method was assessed in ultrasound simulations of a simple numerical phantom and an

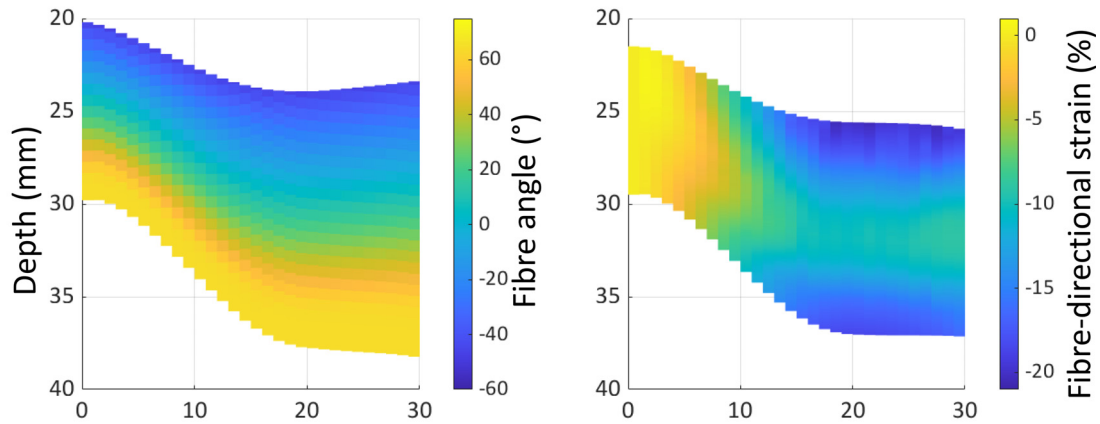
FE model of left ventricular mechanics. Accuracy of fibre orientation and fibre-directional strain estimation was high; however, overall strain imaging performance was low in the FE model phantom. Finally, given the simulation-only format of this study, the eventual utility of the present method must still be assessed in both *ex vivo* experiments and *in vivo* studies.

Similar simulation frameworks have been used to replicate the motion and deformation of the ventricle in the validation of ultrasound strain imaging algorithms (Luo et al. 2009). The finite-element model used as the basis for the present study utilised an idealised geometry and was circumferentially symmetric. Given the small volume of the LV wall that was simulated, a more geometrically and anatomically complex model was not necessary. However, if the present framework was to be expanded, a more anatomically correct model (e.g., biventricular, fibre orientations determined using diffusion-tensor magnetic resonance imaging) would allow detailed validation of fibre orientation and strain at regions of interest in the LV, particularly the septal wall and apex.

Fibre orientation

Good agreement in fibre orientation estimation has previously been reported by both Papadacci et al. (2017), who validated the present method using histology of *ex vivo* porcine myocardium, and Ramalli et al. (2018) in ultrasound simulations. The former estimated orientation from coherently compounded volumes created with steered plane waves, whilst the latter used un-reconstructed channel data,

Ground truth



Estimated

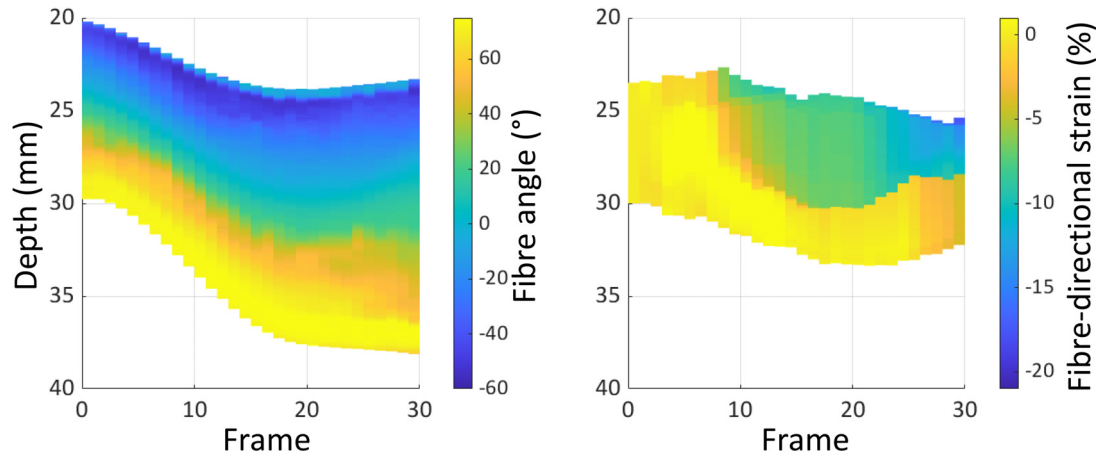


Fig. 6. Change in transmural ground truth (upper) and estimated (lower) fibre angle and fibre-directional strain during systole.

obtained with single plane wave transmission. The present study introduced a confounding factor to the simulations: out-of-plane rotation of the fibres (also present in the *ex vivo* tissue samples). The technique of Ramalli results in a uniform spatial resolution in the region bounded by the aperture, and can allow for calculation of fibre orientation at greater depths, provided all structures are absolutely perpendicular to the beam axis. Structures that are not perpendicular will appear as incoherent signals across the transducer elements. However, structures outside the aperture cannot be resolved and actively corrupt returning (spatially coherent) signals, as their origin cannot be determined. The spatial resolution obtained by compounding steered plane waves is similarly uniform within the Fresnel distance, as the method allows for the focusing of waves at any arbitrary point. Furthermore, steering of plane waves yields a narrow point spread function (improving lateral and elevational resolution), which means that structures outside of the aperture may be imaged and that the out-of-plane orientation of non-

perpendicular structures can be resolved using 3-D BTI (Turquin et al. 2019), although this last step was not performed in this study. However, signals at greater depths or outside the region bounded by the aperture are of a significantly lower SNR and contrast-to-noise ratio. This is due to the side and grating lobes of plane waves and the spreading of the wavefront. In particular, wavefront spreading leads to a larger point spread function, which reduces the precision with which structures can be resolved.

In comparison to Papadacci et al. (2017), the aim of the present study was to estimate the general fibre orientation at a given depth, rather than determine the disarray of cardiac fibres. Similarly, the fractional anisotropy was employed here to give a measure of the reliability of estimates (*i.e.*, how spatially coherent reflections at a given depth were), rather than as an additional measure of fibre disarray.

Significant challenges will be faced in performing accurate estimation of fibre orientation *in vivo*: the

method relies on a good-quality, high-SNR signal received by each element for accurate results. At present, ultrasound systems that can acquire these signals simultaneously in all elements remain expensive, and their use is limited to laboratory or sparse volunteer/clinical measurements.

Additionally, the transducer configuration used in this study would be unable to accurately measure the fibre orientation in a transthoracic echo. In adults, the distance between the transducer and LV wall is typically greater than 40 mm, and therefore, outside the depth at which we observed orientation can be accurately estimated. However, the exact depth at which this occurs has not been investigated here, and there may instead be a more gradual transition from coherence to incoherence when moving out of the region in which steered plane waves fully overlap. Notably, the validation of fibre orientations in the study by Papadacci et al. (2017) was performed at a depth of 15 mm, with the histological samples being 25 mm thick, that is, within the accurately estimated depth range. This means use of the method is restricted to *in vitro* or *ex vivo* experimental setups, such as those used in Ferraiuoli et al. (2019) and Fixsen et al. (2020), until larger-aperture matrix-array transducers with individually addressable elements are available.

It is unlikely that use of diverging waves would increase the maximum depth at which fibre orientation could be accurately estimated; at larger depths, the relative difference in insonification angle for a given point in the volume will be lower; and, given the method's reliance on a high SNR, diverging waves would lower the intensity throughout the volume (although allowing an overall larger volume to be imaged).

Strain imaging and fibre-directional strain

There was a large amount of error between the ground truth and estimated strains in the FE phantom, predominantly when displacements occurred in the axial direction. In all cases displacements were underestimated, meaning poor tracking of the phantom led to inaccurate estimation of strains. For the ideal phantom, two sources of error were identified that explain the difference in the gradient of fibre-directional strain over depth. Firstly, as can be seen in Figure 1D, the start and end of the phantom in the reconstructed volume are dominated by large echoes. These echoes are of a greater amplitude than the underlying speckle that is tracked by the displacement tracking algorithm and, therefore, reduce the accuracy of the tracking (and, therefore, strain estimation). This is evidenced by the larger error at either end of the phantom in Figure 3. Secondly, RMSE for the estimation of fibre orientation was 6.66° over the entire depth of the phantom. Any error in this parameter

directly affects the accuracy of fibre-directional strain calculation.

It is likely then that displacement estimates in the normal directions are too noisy, resulting in the large error in normal strains (other than in the lateral direction). Noise in displacement estimates (*i.e.*, under- and overestimation of interframe displacements throughout the displacement field) can have a number of causes, in particular, a low spatial or temporal resolution or low SNR in the imaged region. Given the high spatial and temporal resolution of the present method and the high amplitude of the scatterers that make up the fibre structures (relative to the randomly placed scatterers), the latter issue is likely a greater contributing factor in the present study. When the strain occurring in other directions is taken (*i.e.*, principal and fibre-directional strains), the ground truth strains are more accurately replicated. By excluding strains that do not occur in the exact principal direction, the erroneous strain estimates caused by poor tracking are effectively filtered out. This is shown particularly by the first principal strain (ee_1). This was closely aligned with the axial direction (and therefore e_z) and yet far more accurately replicated both the shape and magnitude of the ground truth strain. For the fibre-directional strain, this was most closely aligned with the x-axis, which was the most accurately estimated of the normal strains.

Although the principal directions were not aligned, the differences between ground truth and estimated directions remained consistent over the period simulated (seen in the relatively low standard deviations). In the ground truth data the first principal strain is aligned with the axial direction, whilst the mean estimated first principal direction was around 36° off-axis, in the positive lateral direction, when taking into account the overlapping sections of the ground truth and estimated data.

In cases where there was a low inter-frame principal strain magnitude estimated, the estimated second and third principal directions would switch (relative to the ground truth directions). This may explain why the estimated principal strain curves and magnitudes are similar to the ground truth, whilst there is a large error in the mean angular distance for the second and third principal directions.

The mismatch in the principal directions, given they are determined from the strain tensor, is caused by errors in the displacement tracking, in turn a result of the design of the FE phantom (this is explored under Limitations). Differences in the axial tracking of the mesh can be seen in Figure 5 (right-hand plots) and mean that the deformation of the FE phantom is not fully captured by the strain estimation algorithm. Sources of error in the present study will not influence future (real-world) bench-top experiments as they are unique to the approach that was taken to

overcome computational limitations that restrict the possible phantom complexity. However, other factors will increase displacement tracking error in bench-top experiments, for example, the addition of electronic noise and speed-of-sound inconsistencies.

Fibre-directional strain has previously been calculated by a combination of diffusion-tensor and 3-D strain-rate tensor magnetic resonance imaging (Tseng et al. 2006). However, this requires measurement of fibre orientation and strain over multiple cardiac cycles, which may not be feasible on patients with mechanical dyssynchrony. Park et al. (2016) calculated myocardial fibre direction in samples obtained from rats by use of 3-D ultrasound strain imaging combined with biaxial testing. By calculating the Green–Lagrange strain-tensor and boundary stresses, the fibre orientation could be determined with high accuracy.

By calculating strain in the fibre direction, the active strain occurring as a result of the contraction of the muscle can be estimated. Additionally, the manner in which myocardial strain is calculated can be (further) standardized, as cardiac myofibres generally have the same orientation distribution patient to patient. Out-of-plane motion and misalignment of the imaging axis leads to error in strain calculation, which could be counteracted through the present approach, whereby the direction in which strain is calculated is found via the data, rather than being reliant on the skill of the sonographer.

Further studies are needed, initially in *in vitro* or *ex vivo* models, to determine the real-world accuracy and utility of the present method. Of particular interest are pathological scenarios, for instance, infarcted tissue (in which myofibre disarray could also be investigated) or LV mechanical dyssynchrony. Additional studies in simulations, making use of alternative frameworks, or greater computing power would allow for the simulation of higher-density models and thereby smaller fibres or a different fibre model entirely.

Limitations

The small aperture size (9.6×9.6 mm) of the simulated transducer meant that accurate fibre orientation estimation was possible only to around 40 mm (based on our observations); this required the phantom to be positioned closer to the transducer than would be possible *in vivo*. The representation of myofibres in this study (specifically the stepwise change in orientation and fixed fibre shape, amplitude, thickness and spacing in the ultrasound simulations) is highly simplified, with both the structure and manner of simulating the change in transmural orientation during systole not accurately reflecting the true microstructure of the myocardium. This is a limitation of the present simulation framework (Field II), in which tissue is modelled as a superposition

of point scatterers, which is very computationally expensive. Accurately modeled fibres would require orders of magnitude more dense phantoms to replicate the microscopic structure. This may not be the case were another framework used. However, the present framework does allow for the deformation of simulated tissues and relocation of fibre structures, a key requirement of this study. Furthermore, the relative amplitude of the fibre and tissue scatterers was a practical consideration and not based on echocardiographic data.

Another simplification caused the poor strain imaging performance in the axial direction: the spatially coherent signals from the myofibres are represented by high-amplitude, regularly spaced scatterers. To maintain the coherence of signals from the fibres and the spatial distribution of fibre angles through the LV wall, these are not deformed. Only the underlying tissue is deformed, to allow for displacement estimation. Instead (as noted in the methods) the fibre sheets are regenerated for each frame in the region. These regions can therefore appear static to the displacement tracking algorithm, leading to the underestimation of axial strain. Resolving this within the current framework would be challenging because (as seen in Fig. 1C) the transmural orientation of fibres changes non-linearly over the simulated period, and given the need to maintain the spatial coherence of signals from the fibre sheets. Despite this limitation, other strains were more accurately estimated. This issue is a limitation of the present study but not of *ex vivo* or *in vivo* data; therefore, the strain imaging portion of the method will perform equally or more accurately in future studies.

CONCLUSIONS

We have reported that simultaneous measurement of LV wall strains and fibre direction is possible in ultrasound simulations based on a finite-element model of LV mechanics. Combination of these measurements allows the estimation of fibre-directional strain, the direction in which local contraction actively occurs in the cardiac muscle. Fibre direction was estimated accurately in our model, although simplifications made to the model to reduce computational time led to inaccurate estimation of normal strains. Despite this, good agreement was found between ground truth and estimated fibre-directional and principal strains. Real-world testing of the method in experimental setups is needed to investigate the utility of the method in pathological scenarios. However, fundamental issues with currently available ultrasound probes precludes the method's ability to accurately determine fibre orientation *in vivo*, as it presently exists.

Acknowledgments—L.S.F. is supported by the European Commission through the H2020 Marie Skłodowska-Curie European Training Network H2020-MSCA-ITN-2014 VPH-CaSE, www.vph-case.eu, GA No. 642612.

Conflict of interest disclosure—The authors declare no conflict of interest that might have influenced the (presentation of the) work described in this article.

REFERENCES

- Amundsen BH, Helle-Valle T, Edvardsen T, Torp H, Crosby J, Lyseggen E, Støylen A, Ihlen H, Lima JAC, Smiseth OA, Slørdahl SA. Noninvasive myocardial strain measurement by speckle tracking echocardiography: Validation against sonomicrometry and tagged magnetic resonance imaging. *J Am Coll Cardiol* 2006;47:789–793.
- Bovendeerd PHM, Huyghe JM, Arts T, van Campen DH, Reneman RS. Influence of endocardial-epicardial crossover of muscle fibers on left ventricular wall mechanics. *J Biomech* 1994;27:941–951.
- Bovendeerd PHM, Kroon W, Delhaas T. Determinants of left ventricular shear strain. *Am J Physiol Heart Circ Physiol* 2009;297:H1058–H1068.
- Chen X, Xie H, Erkamp R, Kim K, Jia C, Rubin JM, O'Donnell M. 3-D correlation-based speckle tracking. *Ultrason Imaging* 2005;27:21–36.
- Crosby J, Amundsen BH, Hergum T, Remme EW, Langeland S, Torp H. 3-D speckle tracking for assessment of regional left ventricular function. *Ultrason Med Biol* 2009;35:458–471.
- Ferraiuoli P, Fixsen LS, Kappler B, Lopata RGP, Fenner JW, Narracott AJ. Measurement of in vitro cardiac deformation by means of 3D digital image correlation and ultrasound 2D speckle-tracking echocardiography. *Med Eng Phys* 2019;74:146–152.
- Fixsen LS, Petterson NJ, Houthuizen P, Rutten MCM, van de Vosse FN, Lopata RGP. Ultrasound-based estimation of remaining cardiac function in LVAD-supported ex vivo hearts. *Artif Organs* 2020;44:E326–E336.
- Hansen DE, Daughters GT, Alderman EL, Ingels NB, Stinson EB, Miller DC. Effect of volume loading, pressure loading, and inotropic stimulation on left ventricular torsion in humans. *Circulation* 1991;83:1315–1326.
- Ho SY. Anatomy and myoarchitecture of the left ventricular wall in normal and in disease. *Eur J Echocardiogr* 2009;10:iii3–iii7.
- Jensen JA. FIELD: A program for simulating ultrasound systems. *Med Biol Eng Comput* 1996;34:351–352.
- Jensen A, Svendsen B. Calculation of pressure fields from arbitrarily shaped, apodized, and excited ultrasound transducers. *IEEE Trans Ultrason Ferroelectr Freq Control* 1992;39:262–267.
- LeGrice IJ, Smaill BH, Chai LZ, Edgar SG, Gavin JB, Hunter PJ. Laminar structure of the heart: Ventricular myocyte arrangement and connective tissue architecture in the dog. *Am J Physiol Heart Circ Physiol* 1995;269:H571–H582.
- LeGrice IJ, Hunter PJ, Smaill BH. Laminar structure of the heart: A mathematical model. *Am J Physiol Heart Circ Physiol* 1997;272:H2466–H2476.
- Lopata RGP, Nillesen MM, Hansen HHG, Gerrits IH, Thijssen JM, de Korte CL. Performance evaluation of methods for two-dimensional displacement and strain estimation using ultrasound radio frequency data. *Ultrason Med Biol* 2009;35:796–812.
- Lopata RGP, Nillesen MM, Thijssen JM, Kapusta L, de Korte CL. Three-dimensional cardiac strain imaging in healthy children using RF-data. *Ultrason Med Biol* 2011;37:1399–1408.
- Luo J, Lee WN, Konofagou EE. Fundamental performance assessment of 2-D myocardial elastography in a phased-array configuration. *IEEE Trans Ultrason Ferroelectr Freq Control* 2009;56:2320–2327.
- Mallart R, Fink M. The van Cittert–Zernike theorem in pulse echo measurements. *J Acoust Soc Am* 1991;90:2718–2727.
- Özarslan E, Vemuri BC, Mareci TH. Generalized scalar measures for diffusion MRI using trace, variance, and entropy: Generalized scalar measures for diffusion MRI. *Magn Reson Med* 2005;53:866–876.
- Papadacci C, Tanter M, Pernot M, Fink M. Ultrasound backscatter tensor imaging (BTI): Analysis of the spatial coherence of ultrasonic speckle in anisotropic soft tissues. *IEEE Trans Ultrason Ferroelectr Freq Control* 2014;61:986–996.
- Papadacci C, Finel V, Provost J, Villemain O, Bruneval P, Gennisson JL, Tanter M, Fink M, Pernot M. Imaging the dynamics of cardiac fiber orientation in vivo using 3D ultrasound backscatter tensor imaging. *Sci Rep* 2017;7:830.
- Park DW, Sebastiani A, Yap CH, Simon MA, Kim K. Quantification of coupled stiffness and fiber orientation remodeling in hypertensive rat right-ventricular myocardium using 3D ultrasound speckle tracking with biaxial testing. *PLoS One* 2016;11:e0165320.
- Ramalli A, Santos P, D'Hooze J. Ultrasound imaging of cardiac fiber orientation: What are we looking at?. *Proc IEEE Int Ultrason Symp* 2018;1–9.
- Ramalli A, Turquin E, Petrusca L. Experimental validation of a novel technique for ultrasound imaging of cardiac fiber orientation. *Proc IEEE Int Ultrason Symp* 2019;2045–2048.
- Stanton T, Leano R, Marwick TH. Prediction of all-cause mortality from global longitudinal speckle strain: Comparison with ejection fraction and wall motion scoring. *Circulation: Cardiovasc Imaging* 2009;2:356–364.
- Taber LA, Yang M, Podszus WW. Mechanics of ventricular torsion. *J Biomech* 1996;29:745–752.
- Tseng WYI, Dou J, Reese TG, Wedeen VJ. Imaging myocardial fiber disarray and intramural strain hypokinesis in hypertrophic cardiomyopathy with MRI. *J Magn Reson Imaging* 2006;23:1–8.
- Turquin E, Petrusca L, Viallon M. Full 3D anisotropic estimation of tissue in ultrasound imaging. *Proc IEEE Int Ultrason Symp* 2019;56–59.
- Voigt JU, Pedrizzetti G, Lysyansky P, Marwick TH, Houle H, Baumann R, Pedri S, Ito Y, Abe Y, Metz S, Song JH, Hamilton J, Sengupta PP, Kolias TJ, D'Hooze J, Aurigemma GP, Thomas JD, Badano LP. Definitions for a common standard for 2D speckle tracking echocardiography: consensus document of the EACVI/ASE/Industry Task Force to standardize deformation imaging. *Eur Heart J Cardiovasc Imaging* 2015;16:1–11.
- Watson SR, Dormer JD, Fei B. Imaging technologies for cardiac fiber and heart failure: A review. *Heart Fail Rev* 2018;23:273–289.